

RESEARCH ARTICLE | AUGUST 17 2023

First-principles property assessment of hybrid formate perovskites

Abduljelili Popoola ; P. S. Ghosh ; Maggie Kingsland; Ravi Kashikar; D. DeTellem; Yixuan Xu; S. Ma ; S. Witanachchi ; S. Lisenkov; I. Ponomareva 

 Check for updates

J. Chem. Phys. 159, 074702 (2023)

<https://doi.org/10.1063/5.0159526>



View
Online



Export
Citation

CrossMark

Articles You May Be Interested In

Hydrogen bonding and proton transfer in small hydroxylammonium nitrate clusters: A theoretical study

J. Chem. Phys. (August 2003)

Hierarchical cobalt-formate framework series with $(4^{12} \cdot 6^3)(4^9 \cdot 6^6)_n$ ($n = 1-3$) topologies exhibiting slow dielectric relaxation and weak ferromagnetism

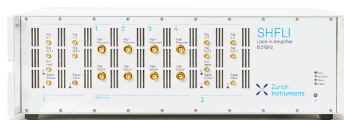
APL Mater (October 2014)

Multiferroic and thermal expansion properties of metal-organic frameworks

J. Appl. Phys. (February 2020)

500 kHz or 8.5 GHz?
And all the ranges in between.

Lock-in Amplifiers for your periodic signal measurements



Find out more

 Zurich
Instruments

First-principles property assessment of hybrid formate perovskites

Cite as: J. Chem. Phys. 159, 074702 (2023); doi: 10.1063/5.0159526

Submitted: 24 May 2023 • Accepted: 19 July 2023 •

Published Online: 17 August 2023



View Online



Export Citation



CrossMark

Abduljelili Popoola,¹ P. S. Ghosh,^{2,3} Maggie Kingsland,¹ Ravi Kashikar,¹ D. DeTellem,¹ Yixuan Xu,⁴ S. Ma,⁴ S. Witanachchi,¹ S. Lisenkov,¹ and I. Ponomareva^{1,a)}

AFFILIATIONS

¹Department of Physics, University of South Florida, Tampa, Florida 33620, USA

²Glass and Advanced Materials Division, Bhabha Atomic Research Centre, Mumbai 400 085, India

³Homi Bhabha National Institute, Anushaktinagar, Mumbai 400 094, India

⁴Department of Chemistry, University of North Texas, CHEM 305D, 1508 W. Mulberry Street, Denton, Texas 76201, USA

^{a)}Author to whom correspondence should be addressed: iponomar@usf.edu

ABSTRACT

Hybrid organic–inorganic formate perovskites, $AB(\text{HCOO})_3$, are a large family of compounds that exhibit a variety of phase transitions and diverse properties, such as (anti)ferroelectricity, ferroelasticity, (anti)ferromagnetism, and multiferroism. While many properties of these materials have already been characterized, we are not aware of any study that focuses on the comprehensive property assessment of a large number of formate perovskites. A comparison of the properties of materials within the family is challenging due to systematic errors attributed to different techniques or the lack of data. For example, complete piezoelectric, dielectric, and elastic tensors are not available. In this work, we utilize first-principles density functional theory based simulations to overcome these challenges and to report structural, mechanical, dielectric, piezoelectric, and ferroelectric properties of 29 formate perovskites. We find that these materials exhibit elastic stiffness in the range 0.5–127.0 GPa; highly anisotropic linear compressibility, including zero and even negative values; dielectric constants in the range 0.1–102.1; highly anisotropic piezoelectric response with the longitudinal values in the range 1.18–21.12 pC/N; and spontaneous polarizations in the range 0.2–7.8 $\mu\text{C}/\text{cm}^2$. Furthermore, we propose and computationally characterize a few formate perovskites that have not been reported yet.

Published under an exclusive license by AIP Publishing. <https://doi.org/10.1063/5.0159526>

I. INTRODUCTION

Hybrid organic–inorganic perovskites (HOIPs) are receiving much attention presently owing to the rapid progress in their synthesis and characterization. They have the chemical formula ABX_3 , where A is typically an organic molecule, B is a metallic cation, and the X site could be a halogen or a molecular linker. They exhibit a variety of phase transitions and a rich range of properties, such as ferromagnetism, (di/ferro)electricity, non-linear optical properties, caloric effects, ferroelasticity, and multiferroicity.^{1,2} Among chemically diverse HOIPs, $AB(\text{HCOO})_3$ is one of the largest families, where one can find most of the aforementioned properties. The structural phase transitions in these materials are primarily driven by the hydrogen bond stabilization and often occur close

to or even above room temperature, which is a highly desirable feature.¹ For example, most ethyl ammonium metal formate perovskites exhibit transitions in the range of 293–400 K.^{3–6} The magnetic properties of formates are mostly determined by weak magnetic interactions mediated by a formate linker, causing them to exhibit magnetic ordering at low temperatures only, typically below 50 K.¹ Furthermore, the $[\text{AZE}][\text{M}(\text{HCOO})_3]$ (AZE = azetidinium; M = Mn^{2+} , Cu^{2+} , and Zn^{2+}) family was reported to have extraordinarily large dielectric constants higher than 10^4 in the vicinity of room temperature.^{7–9} Often, the value exhibits a strong frequency dependence, which resembles the behavior of ferroelectric relaxors.¹⁰ Many formates undergo transitions into polar space groups and, therefore, are possible candidates for ferroelectricity, which is defined by the presence of spontaneous electric

polarization reversible by an electric field. However, the value of spontaneous polarization is typically below $5 \mu\text{C}/\text{cm}^2$, which makes its experimental measurement very challenging.¹¹ The simultaneous realization of ferroelectricity, ferromagnetism, and/or ferroelasticity in some hybrid formates classifies them as multiferroics. It was shown that DMA-Zn(HCOO)₃ becomes multiferroic on substitution of Zn with transition metals, such as Ni, Mn, Co, and Fe.^{2,12,13} DMA-Co(HCOO)₃ is another hybrid in which multiferroicity has been observed.¹⁴ All abbreviations for the A sites used in this study are listed in Table I.

Some formates, including Gua-Mn(HCOO)₃ and DMA-Mn(HCOO)₃, were found to exhibit ferroelasticity.¹⁵ For example, it was experimentally shown that (CH₂)₃NH₂Mn(HCOO)₃ exhibits a ferroelastic transition at 272 K.¹⁶ Mechanical properties have been investigated for several members of formate families and are reviewed in Ref. 17. The exotic negative linear compressibility, defined as an increase in lattice parameter(s) under hydrostatic pressure, has computationally been predicted in HAZ-M(HCOO)₃ (M = Mn, Fe, and Co)^{18,19} and NH₄Zn(HCOO)₃.²⁰ The negative linear compressibility finds applications in pressure sensors and actuators and possibly in the design of artificial muscles.²¹

Evidence of pyroelectricity has been reported in some hybrid formate perovskites. For instance, the pyroelectric coefficient was measured to exhibit a maximum of $5.16 \times 10^{-2} \text{ C}/\text{m}^2 \text{ K}$ under a poling electric field of 7.7 kV/cm at 192 K for DMA-Mn(HCOO)₃.²² In another instance, the pyroelectric current was reported and used to study the order-disorder transition under different pressures in DMA-Co(HCOO)₃.²³ Some other hybrid formate perovskites in which pyroelectric current has been measured include DMA-Mg(HCOO)₃,²⁴ DMA-Mn(HCOO)₃, DMA-Mn_{0.5}Ni_{0.5}(HCOO)₃,^{25,26} Gua-Cu(HCOO)₃,²⁷ CH₃NH₂NH₂Mn(HCOO)₃,²⁸ and DMA-Zn(HCOO)₃.²⁹ The dependence of pyroelectric current on the applied magnetic field has also been demonstrated in DMA-Ni(HCOO)₃.³⁰

Although the aforementioned studies highlight the outstanding progress that has been made in the characterization of these materials, the survey also reveals a scarcity of such investigations, especially in light of the fact that the formate subgroup hosts at least 64 known members.^{1,31,32} It should also be recognized that many such characterizations, spontaneous polarization for example, are rather challenging experimentally. On the other hand, computational investigation is a relatively inexpensive, reliable, and efficient tool to overcome these challenges and achieve a comprehensive assessment of structural, piezoelectric, dielectric, and elastic properties for a wide range of materials in the formate family.

Therefore, in this study, we aim (i) to predict structural parameters, polarization, piezoelectric coefficients, dielectric constants, and elastic stiffness of 29 formate compounds using first-principles

density functional theory (DFT) based simulations; (ii) to provide a comprehensive comparative assessment of the aforementioned properties; and (iii) to catalog the properties that could aid the screening of promising materials.

II. COMPUTATIONAL METHODOLOGY

Table II lists the hybrid formates that we have investigated and the associated experimental references from which the structures have been retrieved along with temperatures at which the structures were recorded. The experimental structures were used to initialize DFT based computations as implemented in the Vienna *Ab initio* Simulation Package (VASP).^{33–36} Technically, all experimental structures were first fully relaxed using the Perdew–Burke–Ernzerhof (PBE) version of the generalized gradient approximation for exchange–correlation functional.³⁷ In order to model hydrogen bonds, we used dispersion corrections of zero-damping D3,^{38,39} which was previously shown to provide good agreement with experimental structures.^{40–44} The electron–ion interactions are treated with the projected augmented wave (PAW) potentials.⁴⁵ We used the plane wave cutoff energy in the range of 700–850 eV and non-Gamma centered k-point mesh, which corresponds to k-point densities in the range of 0.19–0.57 Å⁻¹. Note that the k-point density and cutoff energy for each material are given in Table S1 of the supplementary material. The unit cell parameters and atomic positions were relaxed until stress and forces are less than 0.1 GPa and 1 meV/Å, respectively. The energy convergence criterion for self-consistent calculations was 10⁻⁶ eV. The crystal polarization is evaluated by the Berry phase method developed by King-Smith and Vanderbilt.^{46,47} We computed the *intrinsic* piezoelectric constants e_{ij} and d_{ij} (in matrix notations) defined as the linear response of the polarization to the applied strain and stress, respectively. The d_{ij} coefficients were obtained from $d_{ij} = e_{ik}(C^{-1})_{kj}$, where C is the single crystal elastic constant matrix. The constants e_{ik} and C_{ij} were computed using the finite difference method as implemented in the VASP.⁴⁸ In case of the systems with strongly localized *d*-orbitals, the DFT+U framework was applied. In the DFT+U method, one needs to supply two parameters—the Hubbard parameter U and the exchange interaction parameter J . In this work, we used the approach developed by Dudarev *et al.*,⁴⁹ where only an effective Hubbard parameter $U_{\text{eff}} = U - J$ enters the Hamiltonian. The following values of U_{eff} were computed using the linear response ansatz of Cococcioni and de Gironcoli⁵⁰ using the PAW approach in the VASP and were utilized: 6.5 eV for Mn, 7.2 eV for Fe, 4.6 eV for Co, and 5.1 eV for Ni.

All structures have been checked for mechanical stability using the generalized Born elasticity criteria developed in Ref. 51 and implemented in Ref. 52.

TABLE I. Abbreviations for the A sites used in this study, following Ref. 1.

Material	NH ₂ NH ₃	C ₂ H ₅ NH ₃	C(NH ₂) ₃	(CH ₃) ₂ NH ₂	CH ₃ NH ₃	NH ₂ CHNH ₂
Abbreviation	HAZ	EA	Gua	DMA	MA	FA

TABLE II. Structural properties and polarizations. The ground state magnetic ordering of magnetic materials is in parentheses, where FM and AFM denote the ferromagnetic and antiferromagnetic orderings, respectively. The data in parentheses are the experimental values taken from the references given in the last column. Materials that do not have an experimentally reported structure are in italics.

Material	Space group	a (Å)	b (Å)	c (Å)	β (deg)	V (Å ³)	μ_B	P (μ_C/cm^2)	T (K)	References
Gua-Mn (AFM)	Pnna	8.42 (8.52)	11.91 (11.98)	9.12 (9.06)	90	915 (925)	4.7	Non-polar	293	53
Gua-Fe (AFM)	Pnna	8.35 (8.42)	11.78 (11.85)	8.98 (8.95)	90	883 (892)	3.8	Non-polar	293	53
Gua-Co (AFM)	Pnna	8.28 (8.33)	11.64 (11.75)	8.99 (8.91)	90	866 (873)	2.8	Non-polar	293	53
Gua-Ni (AFM)	Pnna	8.24 (8.26)	11.63 (11.64)	8.91 (8.83)	90	853 (850)	1.8	Non-polar	293	53
Gua-Cu (AFM)	Pna2 ₁	8.50 (8.52)	9.07 (9.03)	11.27 (11.35)	90	869 (874)	0.6	(0, 0, 0.21) (0.11–0.37)	285	27, 53, and 54
Gua-Zn	Pnna	8.27 (8.35)	11.66 (11.73)	8.99 (8.91)	90	868 (872)	0.0	Non-polar	293	53
HONH ₃ -Mn (AFM)	P2 ₁ 2 ₁ 2 ₁	7.80 (7.81)	8.04 (7.96)	13.06 (13.17)	90	819 (819)	4.5	Non-polar	293	55
HONH ₃ -Co (AFM)	P2 ₁ 2 ₁ 2 ₁	7.67 (7.68)	7.82 (7.76)	13.00 (13.02)	90	780 (776)	2.7	Non-polar	293	55
HONH ₃ -Ni (AFM)	P2 ₁ 2 ₁ 2 ₁	7.59 (7.62)	7.98 (7.78)	12.80 (12.73)	90	775 (755)	1.8	Non-polar	293	55
HONH ₃ -Fe (AFM)	P2 ₁ 2 ₁ 2 ₁	7.70	8.00	13.05	90	802	3.6	Non-polar
HONH ₃ -Zn (AFM)	P2 ₁ 2 ₁ 2 ₁	7.65 (7.69)	7.83 (7.74)	13.18 (13.02)	90	790 (775)	0.0	Non-polar	293	55
HONH ₃ -Mg (AFM)	P2 ₁ 2 ₁ 2 ₁	7.67 (7.69)	7.89 (7.79)	12.73 (12.86)	90	770 (770)	0.0	Non-polar	293	55
HAZ-Co (AFM)	Pna2 ₁	8.63 (8.65)	7.74 (7.76)	11.46 (11.55)	90	765 (776)	2.7	(0, 0, 2.81) (2.61 at 405 K)	298	56
HAZ-Mn (FM)	Pna2 ₁	8.99 (8.93)	7.83 (7.82)	11.66 (11.69)	90	820 (817)	4.7	(0, 0, 2.51) (3.58 at 110 K)	110	57
HAZ-Zn	Pna2 ₁	8.65 (8.66)	7.75 (7.72)	11.49 (11.48)	90	771 (768)	0.0	(0, 0, 2.59) (2.6–3.48 at 0–110 K)	110	57 and 58
HAZ-Mg	Pna2 ₁	8.87	7.63	11.45	90	775	0.0	(0, 0, 2.90) (3.44 at 400 K)	...	57
HAZ-Mg	P2 ₁ 2 ₁ 2 ₁	8.00 (7.89)	13.90 (13.75)	7.28 (7.38)	90	809 (802)	0.0	Non-polar	110	57
NH ₄ -Co (AFM)	P ₃	12.54 (12.59)	12.54 (12.59)	8.34 (8.22)	90	1136 (1128)	2.6	(0, 0, 2.35)	110	59
NH ₄ -Fe (AFM)	P ₆ ₃	12.58 (12.62)	12.58 (12.62)	8.57 (8.36)	90	1174 (1153)	3.8	(0, 0, 2.41)	110	59
NH ₄ -Mn (AFM)	P ₆ ₃	12.55 (12.67)	12.55 (12.67)	8.71 (8.54)	90	1189 (1187)	4.5	(0, 0, 2.45)	110	59
NH ₄ -Zn	P ₆ ₃	12.56 (12.59)	12.56 (12.59)	8.38 (8.20)	90	1144 (1126)	0.0	(0, 0, 2.43) (0.93–1.03 at 120–163 K)	110	59–61
MA-Co (AFM)	Pnma	8.18 (8.28)	11.67 (11.67)	8.28 (8.15)	90	790 (789)	2.8	Non-polar	135	62
MA-Co (AFM)	P2 ₁ /c	8.25 (8.18)	11.69 (11.67)	8.20 (8.15)	93.6 (91.9)	789 (789)	2.8	Non-polar	45	62
MA-Mn (AFM)	Pnma	8.39 (8.68)	11.93 (11.95)	8.42 (8.17)	90	843 (847)	4.7	Non-polar	290	63
MA-Mn (AFM)	P2 ₁ /c	8.41	8.47	14.12	121.9	853	4.7	Non-polar
MA-Ni (AFM)	Pnma	8.15 (8.18)	11.62 (11.52)	8.24 (8.08)	90	781 (762)	1.8	Non-polar	100	64
MA-Zn	Pnma	8.31 (8.41)	11.69 (11.71)	8.17 (8.10)	90	794 (798)	0.0	Non-polar	135	63
MA-Zn	P2 ₁ /c	8.27	13.89	8.26	122.4	802	0.0	Non-polar
DMA-Co (AFM)	Cc	14.10	8.24	8.62	121	859	2.7	(6.93, 0, 2.70) (0.3 at 125 K)	...	23
DMA-Mn (AFM)	Cc	14.35 (14.35)	8.39 (8.32)	8.86 (8.88)	120.3	922 (912)	4.7	(7.10, 0, 2.48) (0.3–2.7 at 150–184 K)	285	22, 25, 26, and 65
DMA-Zn	Cc	14.13	8.24	8.64	120.71	865	0.0	(7.30, 0, 2.66) (0.45 at 125 K)	...	29
EA-Mg	Pna2 ₁	8.82 (8.90)	8.12 (8.12)	11.73 (11.81)	90	840 (853)	0.0	(0, 0, 1.45) (3.34 at 93 K)	292	3
FA-Mn (AFM)	C2/c	13.12 (13.44)	8.86 (8.68)	8.23 (8.41)	118.1	859 (865)	4.7	Non-polar	110	66

III. RESULTS AND DISCUSSION

A. Structure

The ground state structural parameters are reported in Table II. A comparison with the experimental data, where available, is also provided in the table. We find that, in most cases, the lattice parameters are within 1% of experimental data (see the supplementary material, Table S1). The pictorial representation of how experimental lattice parameters compare with computational ones is shown in Fig. 1. The figure reveals good agreement between the experiment and computations. We thus conclude that our computational approach provides reliable structural predictions. The ground state structures are available from Ref. 67.

Note that we also augmented our list of HOIPs with the following structures: DMA-Zn, DMA-Co, HONH₃-Fe, and Pna2₁ phase of HAZ-Mg, which so far have not been reported experimentally. Such structures were obtained by replacing Mn in DMA-Mn with Zn or Co, Mn in HONH₃-Mn with Fe, and Zn in HAZ-Zn with Mg, followed by full structural relaxation. These hypothetical structures are in italics in Table II. The majority of the fully relaxed HOIP structures retained their experimental space groups. However, there were some exceptions. The experimental structures of MA-Co are available in both Pnma and P2₁/c phases,⁶² whereas the experimental structures of MA-(Mn,Zn) are available only in the Pnma phase. Our computations predicted that MA-(Mn, Zn, Co)

are mechanically unstable in the Pnma phase, while the P2₁/c phase of MA-Co is mechanically stable. To ensure the mechanical stability of MA-(Mn, Zn), we deformed the Pnma structure along the eigenvector associated with the negative value of C_{44} and subjected such a deformed structure to full structural relaxation, which resulted in the P2₁/c ground state structure. It is, therefore, plausible that these materials may undergo another structural phase transition to the P2₁/c phase at low temperatures. Indeed, experimentally, MA-Co exhibits Pnma phase at room temperature and undergoes a phase transition to P2₁/c at low temperatures.⁶² Both P2₁/c and Pnma phases of MA-(Mn,Zn,Co) are reported in Table II and Ref. 67. However, the dielectric and mechanical properties were calculated from the P2₁/c phase of the structures. The mechanical instability of the experimentally observed finite-temperature phases could tentatively be attributed to the limitations of DFT to the prediction of ground state phases. At least within the chosen level of theory, DFT fails to reproduce some experimental structures obtained at a finite temperature.

It has been reported in previous experimental studies that at low temperatures, DMA-Zn crystallizes in space group Cc with no partial occupancy at N position and possesses a crystal structure similar to DMA-Mn.¹³ However, no structural file has been provided. Therefore, we have initiated our calculation for DMA-Zn by replacing Mn with Zn in experimentally reported DMA-Mn.²⁵ In the case of HAZ-Mg, a previous experimental study reports a non-polar

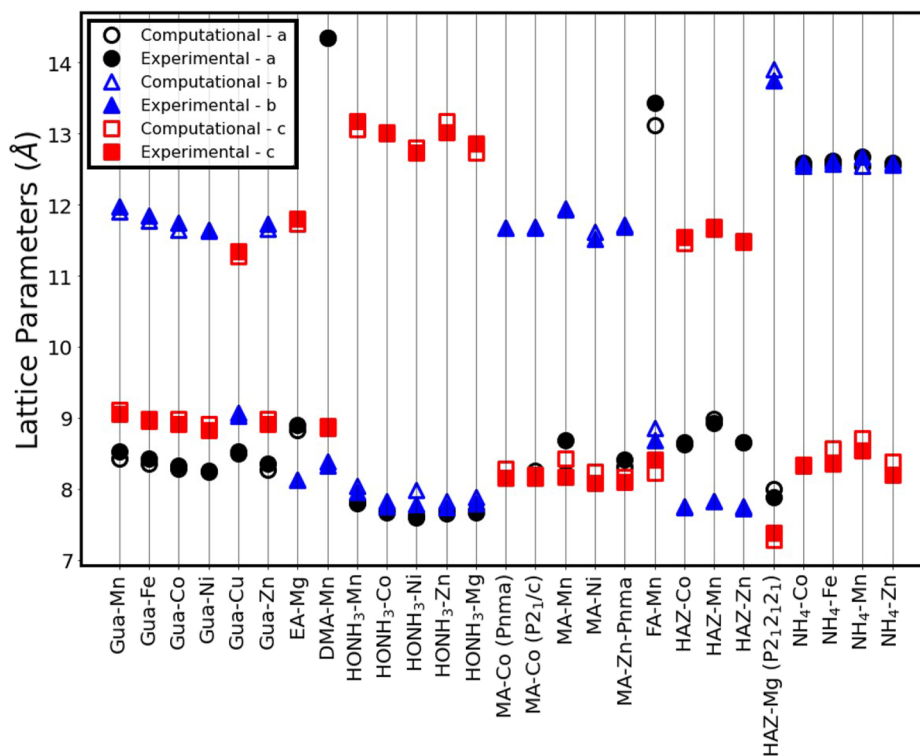


FIG. 1. Comparison between the computational and experimental lattice parameters. Only the structures whose space group is the same for both computations and experiments are compared.

crystal structure $P2_12_12_1$,⁵⁷ but a recent DFT study⁶⁸ shows that the entropy driven effects are responsible for stabilizing the structure in the $Pna2_1$ space group. Therefore, we have initiated our calculation for the $Pna2_1$ phase of HAZ-Mg by replacing Zn with Mg in the experimentally reported $Pna2_1$ phase of HAZ-Zn.⁵⁷

NH_4 -Co is experimentally reported in the $P6_3$ space group at low temperatures. However, a relaxed structure in the same space group was found to be mechanically unstable, so further relaxation resulted in the $P3$ space group.

For all structures with transition metal atoms, we computed energies for different magnetic orderings and selected the one with

the lowest energy as the ground state. It should be noted that in agreement with previous studies,^{18,19,41} we find only very small differences in energy between structures with different magnetic orderings. The magnetic orderings are given in Table II.

B. Polarization

Table III provides the polarization values from the literature and the conditions under which they were reported/computed. The typical values are below $5 \mu C/cm^2$. An inherent periodicity of crystal lattice makes polarization, P , a multivalued quantity. To overcome

TABLE III. Polarizations from the literature. A = $NH_3CH_2CH_3$, P = $PH_3CH_2CH_3$, AF = $NH_3CH_2CF_3$, and PF = $PH_3CH_2CF_3$.

Material	Type	P ($\mu C/cm^2$)	Conditions
A-Mn	Comp.	1.80 ⁷¹	T = 0 K
P-Mn	Comp.	1.00 ⁷¹	T = 0 K
AF-Mn	Comp.	5×10^{71}	T = 0 K
PF-Mn	Comp.	5.90 ⁷¹	T = 0 K
DMA-Mn	Expt.	0.30 ⁶⁵	T = 150 K; B = 9 T (during growth)
	Expt.	2.70–3.61 ^{25,26}	T = 150 K; B = 0–5 T; E = 5 kV/cm
	Expt.	0.8–2.4 ²²	T = 184 K; E = 3.1–7.7 kV/cm
DMA-Ni	Expt.	0.42–0.52 ³⁰	T = 150 K; B = 0–10 T
DMA-Co	Expt.	0.30 ²³	T = 125 K
DMA-Zn	Expt.	0.45 ²⁹	T = 125 K
NH_4Mn	Expt.	0.97 ⁵⁹	T = 140 K
NH_4Mg	Expt.	1.15 ³	T = 93 K
NH_4Zn	Expt.	0.02–0.93 ⁶¹	T = 120–248 K
	Expt.	4.00 ⁷²	T = 273 K; P = 1.44 GPa
	Expt.	1.03 ^{59,60}	T = 163 K
NH_4Sc	Comp.	3.71 ⁷³	T = 0 K
NH_4Ti	Comp.	2.46 ⁷³	T = 0 K
NH_4V	Comp.	2.40 ⁷³	T = 0 K
NH_4Cr	Comp.	2.51 ⁷³	T = 0 K
NH_4Mn	Comp.	2.38 ⁷³	T = 0 K
NH_4Fe	Comp.	2.37 ⁷³	T = 0 K
NH_4Co	Comp.	2.36 ⁷³	T = 0 K
NH_4Ni	Comp.	2.17 ⁷³	T = 0 K
NH_4Cu	Comp.	2.20 ⁷³	T = 0 K
NH_4Zn	Comp.	2.30 ⁷³	T = 0 K
$CH_3NH_2NH_2Mn$	Expt.	0.14 ²⁸	T = 150 K; B = 10 T
$NH_3(CH_2)_4NH_3Mg_2$	Expt.	1.51 ³	T = 93 K
HAZ-Mn	Expt. (estimated)	3.58 ⁵⁷	T = 110 K
HAZ-Co	Expt. (estimated)	2.61 ⁵⁷	T = 405 K
HAZ-Zn	Expt. (estimated)	3.48 ⁵⁷	T = 110 K
HAZ-Mg	Expt. (estimated)	3.44 ⁵⁷	T = 400 K
	Comp.	2.6 ⁵⁸	T = 150–375 K
EA-Mg	Expt. (estimated)	3.43 ³	T = 93 K
Gua-Cr	Comp.	0.22 ⁷⁴	T = 0 K
Gua-Cu _{0.5} Mn _{0.5}	Comp.	9.90 ⁷⁵	T = 0 K
Gua-Cu	Comp.	0.11–0.37 ^{27,54}	T = 0 K

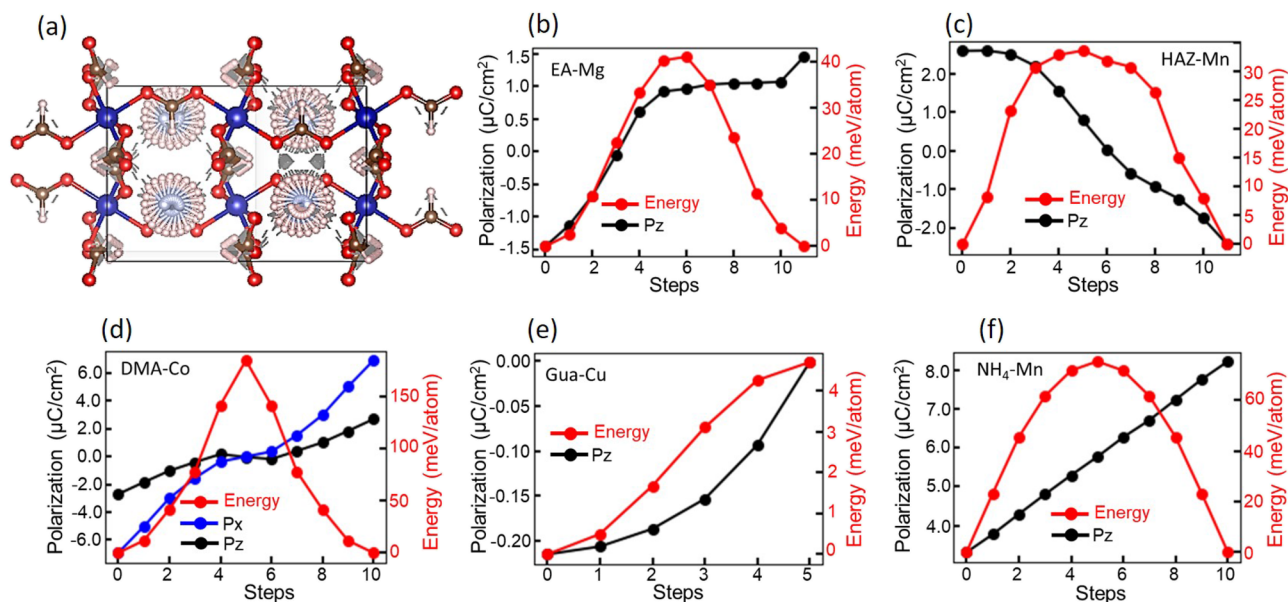


FIG. 2. Structural evolution along the roto-distortion path schematically shown by overlapping structures along the path (a). Variation of polarization and energy along the path for a representative of each family, as given in the legend (b)–(f).

this challenge, the polarization is typically computed along a distortion path that connects the polar structure to the non-polar one.⁶⁹ However, for the case of HOIP, the non-polar high symmetry structure is typically associated with partial occupancy and, therefore, cannot be used as a reference point. One approach to construct the non-polar phase was suggested in Ref. 70. Another approach is to model experiments, where the polarization is obtained from the measurement during its reversal. Such an approach was used in Refs. 41 and 43, where the polarization reversal was achieved from the creation of an inverted structure and generation of a roto-distortion path between the structure and its inversion. The inversion was applied with respect to the inversion center of the high symmetry experimental structure, where available, or with respect to the B site.

The roto-distortion path consists of distortion of the framework and rotation of the A site molecule. We used the same approach for EA-M, HAZ-M, and DMA-M as these compounds have an inversion center in their high temperature phase. An example of polarization evolution along such a path is shown in Figs. 2(b) and 2(c).

For Gua-Cu, the rotation of the Gua molecules resulted in metallic structures, which did not allow for polarization calculations. So, we created a non-polar structure using the pseudosymmetry module of Bilbao Crystallographic Server⁷⁶ and generated a distortion path between the polar and non-polar structures. The polarization along such a path is shown in Fig. 2(e). For the NH₄-M family, the high temperature high symmetry structure is P6₃22, which does not have an inversion center. In this case, we used the U2 axis of

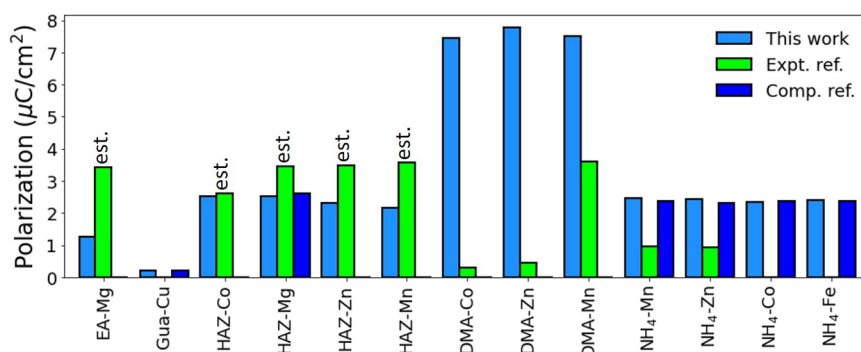


FIG. 3. Comparison of our computational polarization values with the experimental and computational results from the literature.^{3,23,29,57,59,61,65,72} Note that "est." indicates that the polarization was estimated from the separation between the positive and negative charges.

P6₃22 to generate the structure with the reversed polarization direction. Technically, we applied the following transformation: $x \rightarrow y$, $y \rightarrow x$, and $z \rightarrow -z$, on the Wyckoff positions of NH₄-M in the P6₃ phase. An example of polarization along such a path is shown in Fig. 2(f). Note that for NH₄-Co, we report polarization for the P6₃ phase, although it was found to be mechanically unstable in calculations. Our motivation is that this is the phase that has experimentally been reported and, therefore, allows us to assess the polarization under experimentally realizable conditions, rather than the ground state. In addition, the two phases differ from each other very slightly, so we expect little difference in polarization.

Polarizations along the roto-distortion paths for all polar materials studied are shown in Fig. S1 of the supplementary material, while the associated structures are given in Ref. 67. The figures also report the energy along the path. The energies are not likely to be physical as no optimization has been performed. However, they do reveal two minima, that is, double-well potential. The typical barrier height is below 200 meV/atom, which is considered surmountable.⁷⁷

Our computational polarizations are reported in Table II, while the comparison of our results with experimental and computationally predicted values available from the literature is shown in Fig. 3. We find excellent agreement between our computational data and the computational data from the literature. However, there exist discrepancies with the experimental data. This could be attributed to the difference in temperature, and in some cases in phase, the difference in the direction of measurement. In our case, we report the value along the polar direction. The data reveal that the polarization values for the formate family are in the range of 0.2–7.8 $\mu\text{C}/\text{cm}^2$ with the largest values found in DMA-M. The values are a factor of ten lower than the ones for prototypical oxide ferroelectrics, including BaTiO₃ and PbTiO₃.⁷⁸

C. Piezoelectric response

The independent components of piezoelectric tensors, e_{ij} and d_{ij} , which are allowed by symmetry, are given in Tables IV and V,

TABLE IV. Piezoelectric stress constants e_{ij} in C/m^2 . Materials that do not have an experimentally reported structure are in italics.

	e_{15}	e_{24}	e_{31}	e_{32}	e_{33}					
Gua-Cu	-0.011	0.069	-0.017	0.018	0.051					
	e_{15}	e_{24}	e_{31}	e_{32}	e_{33}					
EA-Mg	-0.261	-0.014	-0.035	-0.045	-0.015					
	e_{11}	e_{12}	e_{13}	e_{15}	e_{24}	e_{26}	e_{31}	e_{32}	e_{33}	e_{35}
<i>DMA-Co</i>	0.065	0.071	0.160	0.077	0.012	-0.009	-0.020	0.025	0.107	0.175
<i>DMA-Mn</i>	0.124	0.129	0.165	0.058	0.041	0.006	-0.004	0.073	0.122	0.187
<i>DMA-Zn</i>	0.112	0.062	0.196	0.114	0.019	-0.017	0.020	0.001	0.141	0.258
	e_{14}			e_{25}			e_{36}			
HONH ₃ -Mn	-0.124			0.003			-0.211			
HONH ₃ -Co	-0.102			-0.027			-0.031			
HONH ₃ -Ni	-0.226			0.103			0.247			
<i>HONH₃-Fe</i>	-0.065			-0.004			-0.135			
HONH ₃ -Zn	-0.097			-0.130			-0.218			
HONH ₃ -Mg	-0.005			-0.002			-0.193			
	e_{15}	e_{24}	e_{31}	e_{32}	e_{33}					
HAZ-Co	-0.185	0.138	-0.012	0.035	-0.054					
HAZ-Mn	-0.143	0.060	0.004	0.037	-0.067					
HAZ-Zn	-0.194	0.104	-0.021	0.028	-0.050					
<i>HAZ-Mg (Pna2₁)</i>	-1.172	0.090	-0.032	0.022	-0.088					
	e_{14}			e_{25}			e_{36}			
HAZ-Mg (P2 ₁ 2 ₁ 2 ₁)	-0.190			-0.074			-0.177			
	e_{14}	e_{15}	e_{31}	e_{33}						
NH ₄ -Co	0.001	-0.057	0.017	0.011						
NH ₄ -Fe	0.078	-0.046	0.037	0.023						
NH ₄ -Zn	0.055	-0.049	0.031	0.019						
NH ₄ -Mn	0.034	-0.069	-0.013	-0.015						

TABLE V. Piezoelectric strain constants d_{ij} in pC/N. Materials that do not have an experimentally reported structure are in italics.

	d_{15}	d_{24}	d_{31}	d_{32}	d_{33}							
Gua-Cu	-1.05	7.36	-1.41	0.39	1.23							
	d_{15}	d_{24}	d_{31}	d_{32}	d_{33}							
EA-Mg	-40.55	-1.24	-0.14	-0.84	0.01							
	d_{11}	d_{12}	d_{13}	d_{15}	d_{24}	d_{26}	d_{31}	d_{32}	d_{33}	d_{35}		
<i>DMA-Co</i>	-2.77	0.18	6.52	7.21	0.59	-0.57	-6.19	1.19	7.37	15.05		
<i>DMA-Mn</i>	-1.29	1.58	7.11	8.16	4.04	2.19	-8.56	2.81	11.29	23.16		
<i>DMA-Zn</i>	-2.34	-1.39	9.15	11.85	1.05	-1.32	-7.10	-0.50	11.46	25.36		
			d_{14}			d_{25}			d_{36}			
HONH ₃ -Mn			-8.06			0.33			-11.01			
HONH ₃ -Co			-5.47			-2.35			-1.25			
HONH ₃ -Ni			-9.65			9.97			11.38			
<i>HONH₃-Fe</i>			-3.66			-0.75			-5.85			
HONH ₃ -Zn			-6.03			-13.16			-10.86			
HONH ₃ -Mg			-0.22			-0.16			-6.47			
			d_{15}			d_{24}			d_{31}	d_{32}	d_{33}	
HAZ-Co			-20.73			14.08			-1.01	1.54	-1.32	
HAZ-Mn			-26.72			6.90			-0.07	1.71	-2.33	
HAZ-Zn			-22.48			10.71			-1.41	1.62	-1.24	
<i>HAZ-Mg (Pna2₁)</i>			-22.40			8.86			-1.53	1.73	-1.74	
					d_{14}			d_{25}			d_{36}	
HAZ-Mg (P2 ₁ 2 ₁ 2 ₁)					-8.91			-3.62			-14.64	
			d_{14}			d_{15}			d_{31}			d_{33}
NH ₄ -Co			0.49			-2.90			0.37			-0.20
NH ₄ -Mn			1.99			-4.09			-3.55			4.00
NH ₄ -Zn			3.07			-2.73			0.71			-0.42
NH ₄ -Fe			4.30			-2.47			1.05			-0.63

respectively. The comparative view is shown in Fig. S2 of the supplementary material. For the formates with the Pna2₁ space group, we mostly find largest values for e_{15} and d_{15} components of the tensor. For materials in the Cc and P2₁2₁2₁ space groups, the largest components are e_{35} (d_{35}) and e_{36} (d_{36}), respectively, and can reach 0.26 C/m² (25.36 pC/N) and 0.18 C/m² (14.64 pC/N) in DMA-Zn and HAZ-Mg, respectively. The longitudinal coefficients along the crystallographic directions, e_{ij} and d_{ij} , $i = 1, 2, 3$, range from 0.01 to 0.14 C/m² and 0.01 to 11.46 pC/N, respectively, with the largest of these values belonging to DMA-Zn. The transverse coefficients e_{ij} and d_{ij} , $i, j = 1, 2, 3$, are in the range 0.00–0.20 C/m² and 0.07–9.15 pC/N, respectively, with the largest values belonging to DMA-Zn.

The directional dependence of the longitudinal piezoelectric stress and strain responses was analyzed using MTEX⁷⁹ and is presented in Figs. 4 and 5, respectively, for a representative material in each family. For all materials, we find the response to be highly anisotropic. The longitudinal piezoelectric stress coefficient can

reach 0.22 C/m² in DMA-Co, while the strain coefficient can reach 12.93 pC/N. 3D visualizations of the piezoelectric stress/strain surfaces for the rest of the materials are shown in Figs. S3 and S4 of the supplementary material.

Thus, our data indicate that the intrinsic piezoelectric strain response in the formate family can reach 26.7 pC/N (in HAZ-Mn) for the shear stress component and 21.12 pC/N for the longitudinal one. The DMA family exhibits the best values.

D. Dielectric response

The symmetry allowed components of the dielectric tensor are reported in Table VI. The typical value is 5. However, the computations predict Gua-M to exhibit distinctively high values, up to 100.00, comparable in order of magnitude to dielectric constants of BaTiO₃.⁸⁰ The comparative view of the dielectric constants is shown in Fig. 6, which confirms that the Gua-M family exhibits the largest response. The nature of such an unusual response deserves further investigation.

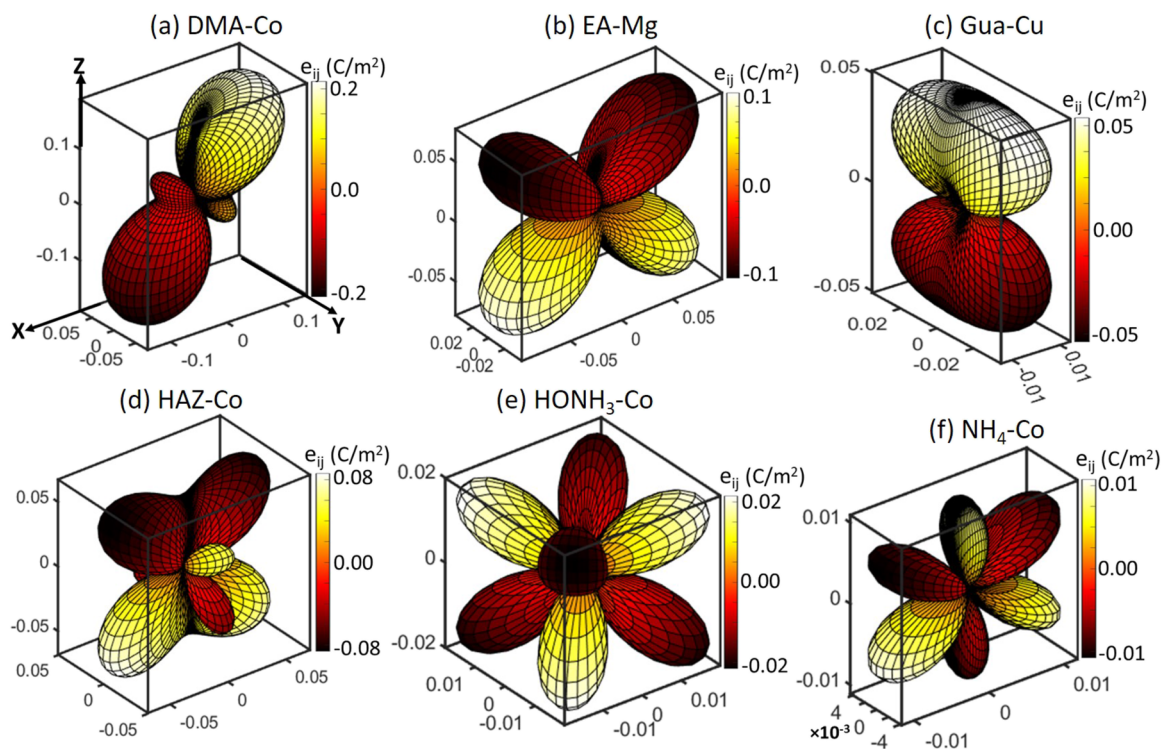


FIG. 4. Piezoelectric stress surface for a representative from each family, as indicated in the titles.

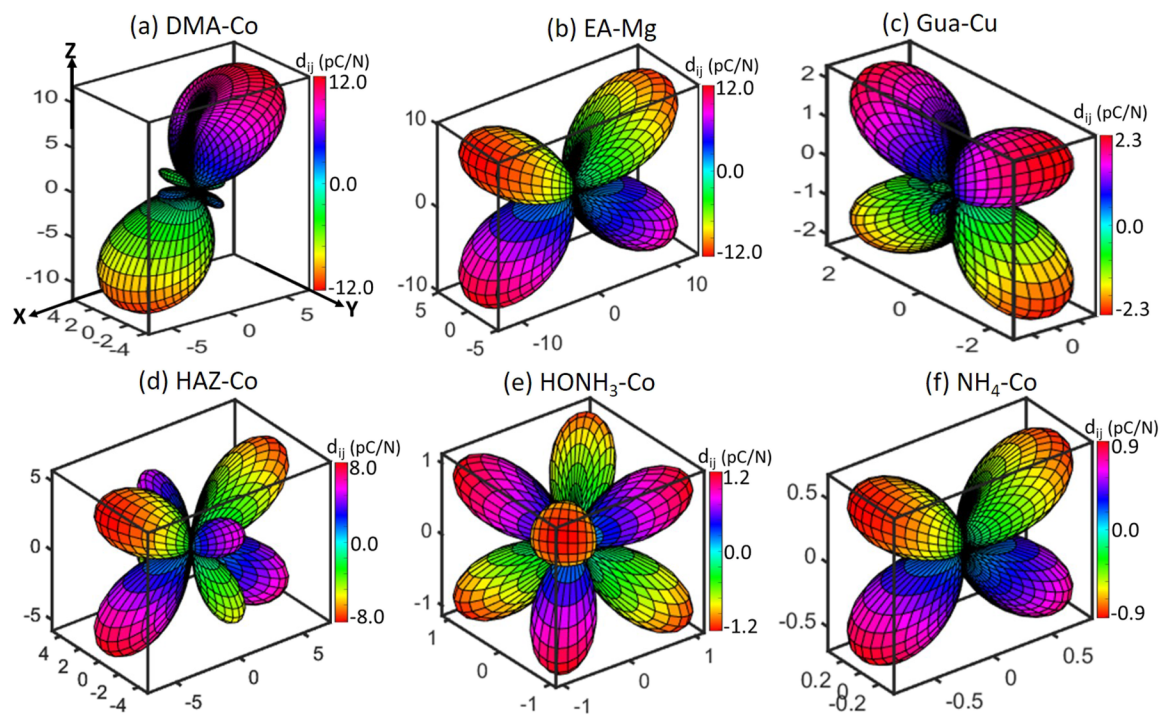


FIG. 5. Piezoelectric strain surface for a representative from each family, as indicated in the titles.

TABLE VI. Dielectric constants. Materials that do not have an experimentally reported structure are in italics.

	ϵ_{11}	ϵ_{22}	ϵ_{33}		
Gua-Mn	5.31	79.19	34.42		
Gua-Fe	4.62	102.12	30.26		
Gua-Co	5.26	67.72	30.55		
Gua-Ni	4.94	73.59	35.51		
Gua-Cu	6.79	6.85	6.26		
Gua-Zn	5.33	5.20	5.68		
	ϵ_{11}	ϵ_{22}	ϵ_{33}		
EA-Mg	4.82	4.63	4.67		
	ϵ_{11}	ϵ_{22}	ϵ_{33}	ϵ_{13}	Expt. Reference
<i>DMA-Co</i>	4.92	4.61	5.35	0.33	
<i>DMA-Mn</i>	4.93	4.53	5.53	0.41	3–6 94
<i>DMA-Zn</i>	5.50	4.98	6.00	0.41	8–10 95
	ϵ_{11}	ϵ_{22}	ϵ_{33}		
HONH ₃ -Mn	5.90	6.04	5.21		
HONH ₃ -Co	5.84	5.93	4.95		
HONH ₃ -Ni	5.56	6.48	5.08		
<i>HONH₃-Fe</i>	5.14	5.29	4.46		
HONH ₃ -Zn	6.26	6.04	5.15		
HONH ₃ -Mg	4.84	5.01	4.43		
	ϵ_{11}	ϵ_{22}	ϵ_{33}	ϵ_{13}	
MA-Co (<i>P2₁/c</i>)	5.21	5.34	5.89	0.22	
<i>MA-Zn (P2₁/c)</i>	5.17	5.83	6.06	-0.20	
<i>MA-Mn (P2₁/c)</i>	4.62	4.85	5.29	-0.13	
MA-Ni (<i>Pnma</i>)	5.21	13.69	5.11		
	ϵ_{11}	ϵ_{22}	ϵ_{33}		
HAZ-Co	4.87	5.05	5.03		
HAZ-Mn	4.66	4.84	4.83		
HAZ-Zn	5.30	5.41	5.49		
<i>HAZ-Mg (Pna2₁)</i>	4.31	4.65	4.50		
HAZ-Mg (<i>P2₁2₁2₁</i>)	5.17	4.75	9.29		
	ϵ_{11}	ϵ_{22}	ϵ_{33}	ϵ_{13}	
FA-Mn	4.36	4.72	5.07	0.27	
	ϵ_{11}	ϵ_{22}	ϵ_{33}		
NH ₄ -Co	5.38	5.38	6.04		
NH ₄ -Fe	4.77	4.77	5.28		
NH ₄ -Mn	5.51	5.51	5.94		
NH ₄ -Zn	5.28	5.28	6.17		

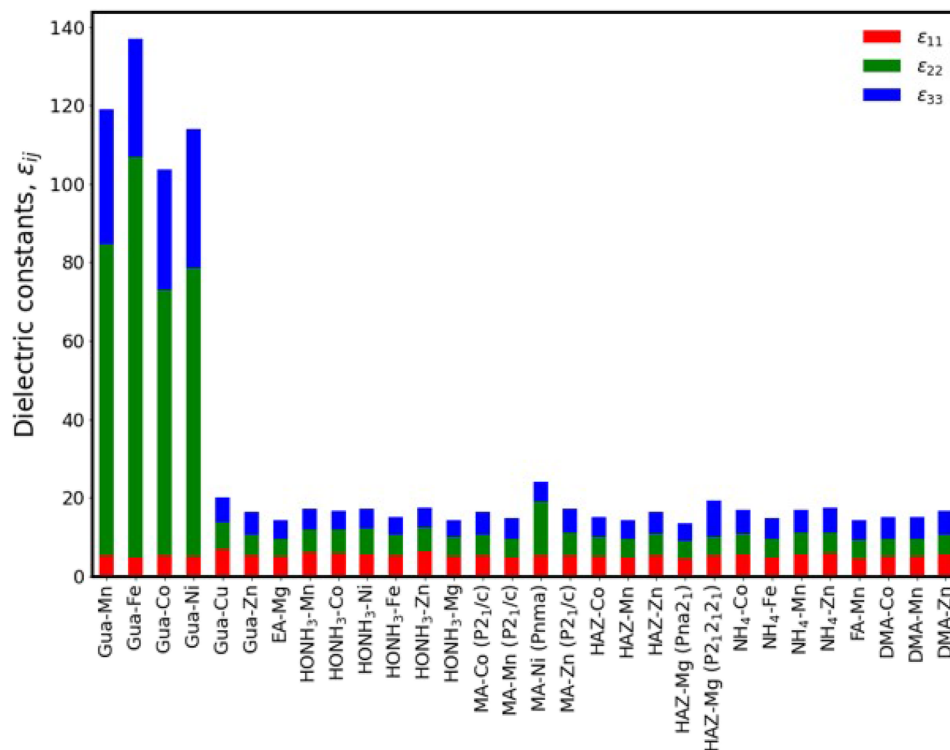


FIG. 6. Comparative view of the components of the dielectric tensor.

E. Mechanical properties

Mechanical properties describe the materials' response to external mechanical stimuli, such as pressure, stress, or strain. Some representative data from the literature for Young's and elastic moduli of formate perovskites are compiled in Table VII. The inde-

pendent components of stiffness tensors computed in this work are given in Table S2 of the supplementary material. They satisfy the Born conditions for the elastic stability^{51,81} as checked by VASPKIT.⁵² The typical diagonal elements are in the range 3.3–127.0. A comparative view of the stiffness tensor components

TABLE VII. Elastic properties from the literature. AZE = $(\text{CH}_2)_3\text{NH}_2$.

Material	Type	Young's modulus (GPa)	Elastic modulus (GPa)	Reference
DMA-Ni	Expt.	24.5		17
DMA-Mn	Expt.	19.0		17
DMA-Co	Expt.	21.5		17
DMA-Zn	Expt.	19.0		17
Gua-Cu	Expt.		15.0–21.0	90
Gua-Zn	Expt.		24.0–29.0	90
Gua-Mn	Expt. and comp.		23.5(6)–28.6(4)	15
AZE-Cu	Expt. and comp.		11.5(4)–12.6(3)	15
HAZ-Zn	Expt.		24.5–26.5	91
HAZ-Mn	Expt.		24.5–28.6	91
NH ₄ Zn	Expt. and comp.		18.2–34.4	20

among all the formates is shown in Fig. S5 of the supplementary material. We computed the average bulk modulus (B), Young's modulus (E), shear modulus (G), Poisson's ratio (ν), and Cauchy's pressure (CP) of bulk polycrystals within Hill's approximation as implemented in VASP^{52,82–87} and report them in Table VIII. The values compare well with the experimental results, listed in Table VII.

Poisson's ratio, defined as the ratio of transverse compressive strain to longitudinal tensile strain, and Pugh's ratio, commonly expressed as the B/G ratio, can be used to characterize the ductility or brittleness of crystals. The former one typically ranges from 0.0 to 0.5. The ductility–brittleness border line is usually drawn at the Poisson's ratio of 0.26 and Pugh's ratio of 1.75.^{88,89} As shown

in Fig. 7, most of the formates studied in this work are ductile and, therefore, are able to withstand large stresses and exhibit malleability.

Figure 8 shows the directional dependence of linear compressibility, defined as linear expansion or compression of materials upon application of isotropic pressure. Interestingly, the data predict that a few formates have negative values (indicated by red color) and some exhibit nearly zero values. For example, HONH₃-Ni, MA-Co, and NH₄-Mn exhibit negative values along the $\langle 010 \rangle$, $\langle 101 \rangle$, and $\langle 001 \rangle$ family of directions, respectively. The directional dependence of linear compressibility of other materials is presented in Fig. S6 of the supplementary material. Previously, a negative linear compressibility was pre-

TABLE VIII. Mechanical properties of formates. B , E , and G are the average bulk, Young's, and shear moduli of bulk polycrystals, respectively. B/G , ν , CP, ALC, LC_{\min} , and LC_{\max} are Pugh's ratio, Poisson's ratio, Cauchy's pressure, anisotropic linear compressibility, minimum linear compressibility, and maximum linear compressibility, respectively. Materials that do not have an experimentally reported structure are in italics.

	B (GPa)	E (GPa)	G (GPa)	B/G	ν	CP (GPa)	ALC	LC_{\min} (TPa ⁻¹)	LC_{\max} (TPa ⁻¹)
Gua-Mn	23.5	28.2	10.8	2.2	0.30	1.5	11.5	2.41	27.04
Gua-Fe	27.4	30.2	11.5	2.4	0.32	1.9	10.2	2.18	22.32
Gua-Co	29.0	35.7	13.8	2.1	0.30	2.0	8.5	2.45	20.87
Gua-Ni	64.1	40.7	14.6	4.4	0.4	35.6	215.6	0.05	10.47
Gua-Cu	26.1	30.0	11.4	2.3	0.3	10.4	5.0	5.03	25.32
Gua-Zn	30.3	34.2	13.0	2.3	0.3	5.0	8.2	2.46	20.04
EA-Mg	33.7	34.2	12.9	2.6	0.33	21.1	1.9	6.72	12.76
<i>DMA-Co</i>	32.5	31.3	11.7	2.8	0.34	11.4	2.6	6.85	17.54
<i>DMA-Mn</i>	20.9	23.8	9.0	2.3	0.32	6.3	3.2	8.51	26.90
<i>DMA-Zn</i>	31.7	28.2	10.4	3.1	0.35	15.3	3.6	5.36	19.55
HONH ₃ -Mn	15.3	27.5	11.5	1.3	0.20	-0.2	3.7	11.33	41.90
HONH ₃ -Co	26.8	36.9	14.5	1.8	0.27	7.0	3.2	7.18	23.08
HONH ₃ -Ni	8.5	21.7	10.1	0.8	0.08	-8.4	-2.2	-188.08	405.43
<i>HONH₃-Fe</i>	22.0	34.0	13.6	1.6	0.24	3.9	3.7	7.63	28.34
HONH ₃ -Zn	28.0	33.8	13.0	2.2	0.30	9.1	2.2	7.51	16.72
HONH ₃ -Mg	24.5	41.2	16.9	1.5	0.22	-0.7	2.7	8.72	23.35
<i>MA-Co (P2₁/c)</i>	19.9	21.1	8.0	2.5	0.32	12.4	-1.8	-32.24	59.26
<i>MA-Mn (P2₁/c)</i>	23.7	23.4	8.8	2.7	0.34	17.8	-210.5	-0.15	32.22
<i>MA-Ni (Pnma)</i>	27.8	23.1	8.5	3.3	0.35	8.6	6.3	1.96	22.48
<i>MA-Zn (P2₁/c)</i>	29.7	27.5	10.2	2.9	0.35	20.9	11.7	4.22	26.36
HAZ-Co	30.1	31.5	11.9	2.5	0.33	18.6	12.6	1.77	22.30
HAZ-Mn	24.8	23.1	8.6	2.9	0.35	15.6	-20.0	-1.73	34.68
HAZ-Zn	28.6	28.8	10.8	2.6	0.33	16.9	32.3	0.82	26.56
<i>HAZ-Mg (Pna2₁)</i>	30.2	31.3	11.8	2.6	0.33	19.6	6.1	3.28	19.88
<i>HAZ-Mg (P2₁2₁2₁)</i>	36.2	34.7	12.9	2.8	0.34	6.6	2.3	5.28	13.56
FA-Mn	22.8	25.4	9.6	2.4	0.32	-6.1	53.6	1.07	58.19
NH ₄ -Co	33.9	32.0	11.9	2.8	0.34	3.9	-9.8	-1.73	16.92
NH ₄ -Fe	29.5	27.8	10.3	2.9	0.34	2.5	-4.7	-4.50	21.31
NH ₄ -Mn	18.5	15.1	5.5	3.4	0.36	0.7	-0.9	-439.63	381.82
NH ₄ -Zn	34.7	31.5	11.7	3.0	0.35	6.2	-8.2	-2.04	16.69

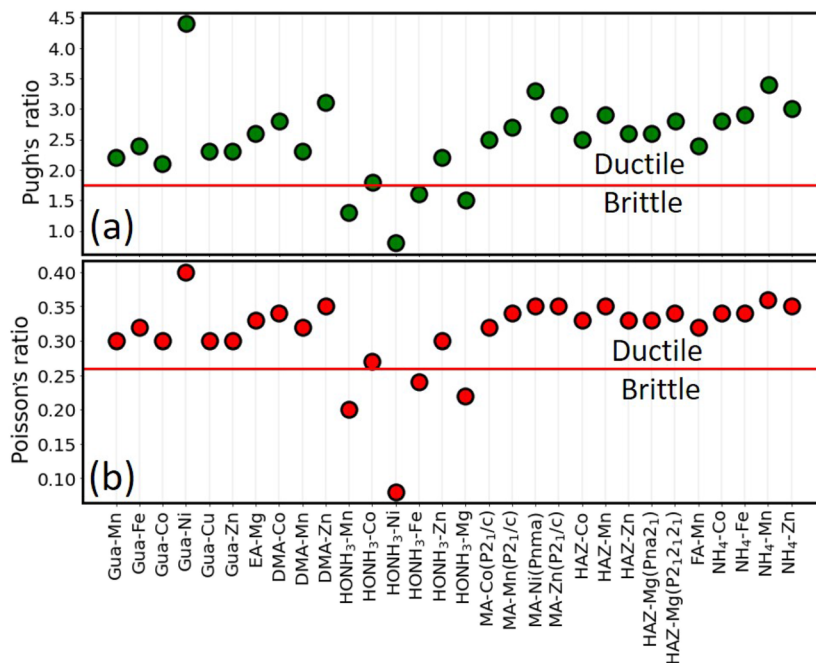


FIG. 7. Pugh's (a) and Poisson's (b) ratios of formates studied in this work.

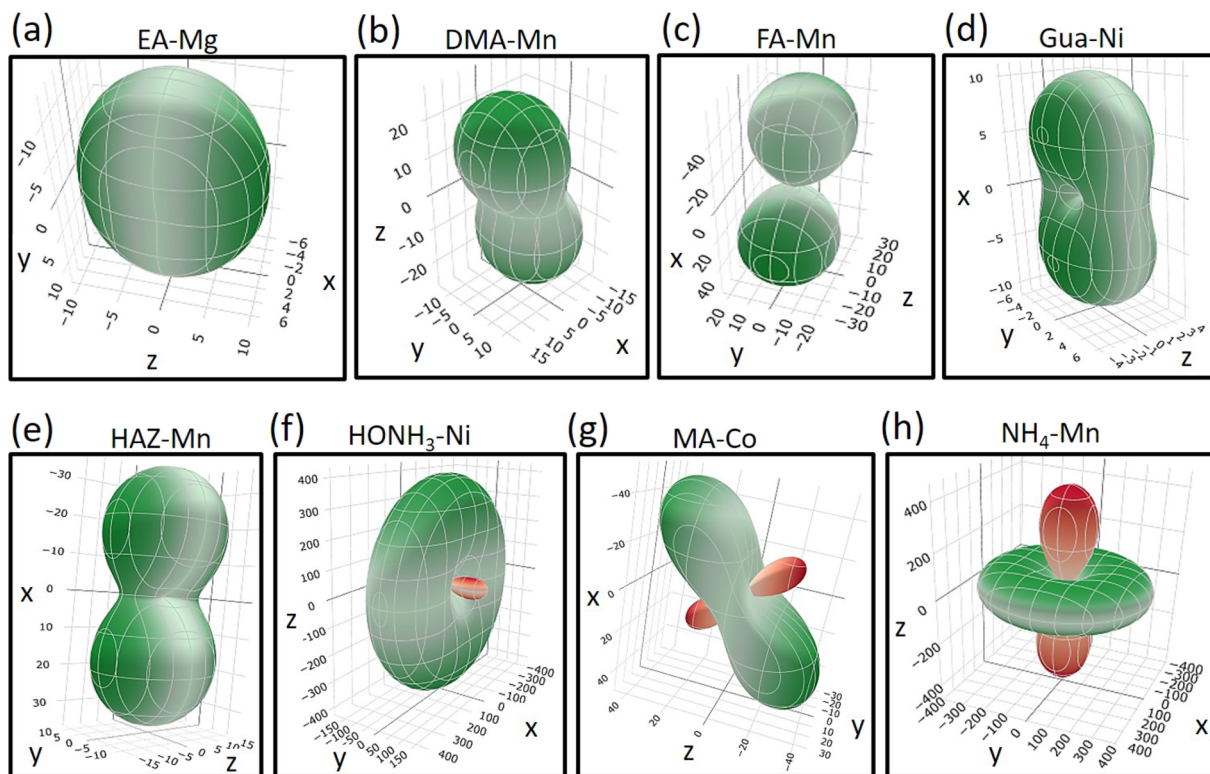


FIG. 8. 3D plots of linear compressibility for a representative material in each family as given in the titles. The green and red colors correspond to the positive and negative values, respectively.

dicted for HAZ-Co, HAZ-Mn, HAZ-Fe, and $\text{NH}_4\text{-Zn}$ ^{18–20} and explained on the basis of the strut-hinge model.^{92,93} In such a model, the formate framework is thought of as made from rigid struts and relatively flexible hinges. As a result, the deformation is highly anisotropic, and in some cases, the rate of hinge deformation overpowers the rate of strut deformation, resulting in the expansion along directions subtended by the hinge. Further investigations into the negative compressibility in these materials are needed to validate our findings and provide additional insights.

IV. CONCLUSION AND OUTLOOK

In summary, we have used DFT computations to assess the structural, electric, piezoelectric, and mechanical properties of 29 hybrid formate perovskites. We predict that the ground state phase of most MA-M (M = Co, Mn, and Zn) formates is different from the low temperature phase reported experimentally, which suggests additional phase transitions at very low temperatures. The spontaneous polarizations range from 0.2 to 7.8 $\mu\text{C}/\text{cm}^2$ with the largest values being in the DMA-M family. They are expected to be reversible by the electric field as the upper estimate for the energy barrier is 200 meV/atom. We also find polarization values often exceeding the experimentally reported ones, which we attribute to the difference in the direction of measurement. Thus, our study could guide toward the optimization of materials' performance. The dielectric constants are typically 5.0. Nevertheless, the Gua family exhibits outstandingly large values in the range 4.6–102.1, which, however, need to be further validated. The intrinsic piezoelectric strain and stress constants are in the range 0.1–25.8 $\mu\text{C}/\text{cm}^2$ and 0.1–26.7 pC/N, respectively. The responses were also found to be highly anisotropic. The components of elastic stiffness tensor range from 0.3 to 127.0 GPa. On the basis of Pugh's and Poisson's ratios, we found most of the materials to be ductile. The computations predict that linear compressibility is highly anisotropic and many materials (e.g., $\text{HONH}_3\text{-Ni}$, $\text{NH}_4\text{-Mn}$, Gua-Ni, and MA-Co) exhibit either zero or even negative values. All computational data are available from Ref. 67.

Our study reveals that additional investigations are needed to validate and explain the outstanding dielectric response of Gua-M formates and the large piezoelectric response of DMA-M formates, along with the large negative compressibility values for $\text{HONH}_3\text{-Ni}$ and $\text{NH}_4\text{-Mn}$. Investigation into the origin of negative and/or nearly zero values of compressibility is also required.

SUPPLEMENTARY MATERIAL

The supplementary material provides additional data, analysis, and visualization of the structural, ferroelectric, piezoelectric, and mechanical properties of hybrid formate perovskites studied in this work.

ACKNOWLEDGMENTS

This work was supported by the National Science Foundation under Grant No. EPMD-2029800.

AUTHOR DECLARATIONS

Conflict of Interest

The authors have no conflicts to disclose.

Author Contributions

Abduljelili Popoola: Conceptualization (equal); Data curation (equal); Formal analysis (equal); Investigation (equal); Methodology (equal); Visualization (equal); Writing – original draft (equal); Writing – review & editing (equal). **P. S. Ghosh:** Conceptualization (equal); Data curation (equal); Formal analysis (equal); Investigation (equal); Methodology (equal); Visualization (equal); Writing – original draft (equal); Writing – review & editing (equal). **Maggie Kingsland:** Conceptualization (equal); Data curation (equal); Formal analysis (equal); Investigation (equal); Methodology (equal); Visualization (equal); Writing – original draft (equal); Writing – review & editing (equal). **Ravi Kashikar:** Conceptualization (equal); Data curation (equal); Formal analysis (equal); Investigation (equal); Methodology (equal); Visualization (equal); Writing – original draft (equal); Writing – review & editing (equal). **D. DeTellem:** Investigation (equal); Writing – original draft (equal); Writing – review & editing (equal). **Yixuan Xu:** Investigation (equal); Writing – original draft (equal); Writing – review & editing (equal). **S. Ma:** Investigation (equal); Writing – original draft (equal); Writing – review & editing (equal). **S. Witanachchi:** Investigation (equal); Writing – original draft (equal); Writing – review & editing (equal). **S. Lisenkov:** Conceptualization (equal); Data curation (equal); Formal analysis (equal); Investigation (equal); Methodology (equal); Supervision (equal); Validation (equal); Visualization (equal); Writing – original draft (equal); Writing – review & editing (equal). **I. Ponomareva:** Conceptualization (equal); Data curation (equal); Formal analysis (equal); Investigation (equal); Methodology (equal); Supervision (equal); Validation (equal); Visualization (equal); Writing – original draft (equal); Writing – review & editing (equal).

DATA AVAILABILITY

The data that support the findings of this study are available in GitHub repository⁶⁷ and from the corresponding author upon reasonable request.

REFERENCES

- W. Li, A. Stroppa, Z. Wang, and S. Gao, *Hybrid Organic-Inorganic Perovskites* (Wiley, 2020).
- Y. Ma and Y. Sun, *J. Appl. Phys.* **127**, 080901 (2020).
- R. Shang, G.-C. Xu, Z.-M. Wang, and S. Gao, *Chem. - Eur. J.* **20**, 1146 (2014).
- R. Shang, S. Chen, B.-W. Wang, Z.-M. Wang, and S. Gao, *Angew. Chem., Int. Ed.* **55**, 2097 (2016).
- M. Ptak, M. Maczka, A. Gagor, A. Sieradzki, A. Stroppa, D. Di Sante, J. M. Perez-Mato, and L. Macalik, *Dalton Trans.* **45**, 2574 (2016).
- M. Ptak, M. Maczka, A. Gagor, A. Sieradzki, B. Bondzior, P. Dereń, and S. Pawlus, *Phys. Chem. Chem. Phys.* **18**, 29629 (2016).
- Y. Imai, B. Zhou, Y. Ito, H. Fijimori, A. Kobayashi, Z.-M. Wang, and H. Kobayashi, *Chem. Asian J.* **7**, 2786 (2012).
- B. Zhou, Y. Imai, A. Kobayashi, Z.-M. Wang, and H. Kobayashi, *Angew. Chem., Int. Ed.* **50**, 11441 (2011).

- ⁹T. Asaji, Y. Ito, J. Seliger, V. Zagar, A. Gradisek, and T. Apih, *J. Phys. Chem. A* **116**, 12422 (2012).
- ¹⁰V. V. Shvartsman and D. C. Lupascu, *J. Am. Ceram. Soc.* **95**, 1 (2012).
- ¹¹K. Asadi and M. A. van der Veen, *Eur. J. Inorg. Chem.* **2016**, 4332.
- ¹²P. Jain, V. Ramachandran, R. J. Clark, H. D. Zhou, B. H. Toby, N. S. Dalal, H. W. Kroto, and A. K. Cheetham, *J. Am. Chem. Soc.* **131**, 13625 (2009).
- ¹³P. Jain, N. S. Dalal, B. H. Toby, H. W. Kroto, and A. K. Cheetham, *J. Am. Chem. Soc.* **130**, 10450 (2008).
- ¹⁴D.-W. Fu, W. Zhang, H.-L. Cai, Y. Zhang, J.-Z. Ge, R.-G. Xiong, S. Huang, and T. Nakamura, *Angew. Chem., Int. Ed.* **50**, 11947 (2011).
- ¹⁵W. Li, A. Thirumurugan, P. T. Barton, Z. Lin, S. Henke, H. H.-M. Yeung, M. T. Wharmby, E. G. Bithell, C. J. Howard, and A. K. Cheetham, *J. Am. Chem. Soc.* **136**, 7801 (2014).
- ¹⁶W. Li, Z. Zhang, E. G. Bithell, A. S. Batsanov, P. T. Barton, P. J. Saines, P. Jain, C. J. Howard, M. A. Carpenter, and A. K. Cheetham, *Acta Mater.* **61**, 4928 (2013).
- ¹⁷J.-C. Tan, P. Jain, and A. K. Cheetham, *Dalton Trans.* **41**, 3949 (2012).
- ¹⁸P. S. Ghosh and I. Ponomareva, *J. Phys. Chem. Lett.* **12**, 7560 (2021).
- ¹⁹P. S. Ghosh and I. Ponomareva, *J. Phys. Chem. Lett.* **13**, 3143 (2022).
- ²⁰W. Li, M. R. Probert, M. Kosa, T. D. Bennett, A. Thirumurugan, R. P. Burwood, M. Parinello, J. A. K. Howard, and A. K. Cheetham, *J. Am. Chem. Soc.* **134**, 11940 (2012).
- ²¹A. B. Cairns and A. L. Goodwin, *Phys. Chem. Chem. Phys.* **17**, 20449 (2015).
- ²²Y. Ma, J. Cong, Y. Chai, L. Yan, D. Shang, and Y. Sun, *Appl. Phys. Lett.* **111**, 042901 (2017).
- ²³Z. Yu, C. Liu, Z. Shen, K. Zhai, D. Xu, A. Nie, J. Xiang, F. Wen, C. Mu, B. Wang, L. Wang, L. Wang, Z. Liu, and Y. Tian, *J. Phys. Chem. Lett.* **11**, 9566 (2020).
- ²⁴S. A. LoCicero, C. M. Averback, U. Shumnyk, E. S. Choi, and D. R. Talham, *J. Phys. Chem. C* **124**, 21113 (2020).
- ²⁵C. Liu, K. Zhai, Z. Yu, A. Nie, Z. Liu, and Y. Sun, *J. Phys. Chem. C* **124**, 16111 (2020).
- ²⁶W. Wang, L.-Q. Yan, J.-Z. Cong, Y.-L. Zhao, F. Wang, S.-P. Shen, T. Zou, D. Zhang, S.-G. Wang, X.-F. Han, and Y. Sun, *Sci. Rep.* **3**, 2024 (2013).
- ²⁷Y. Tian, A. Stroppa, Y.-S. Chai, P. Barone, M. Perez-Mato, S. Picozzi, and Y. Sun, *Phys. Status Solidi RRL* **9**, 62 (2015).
- ²⁸M. Maczka, A. Gagor, M. Ptak, W. Paraguassu, T. A. da Silva, A. Sieradzki, and A. Pikul, *Chem. Mater.* **29**, 2264 (2017).
- ²⁹M. Simenas, S. Balciunas, M. Maczka, J. Banys, and E. E. Tornau, *Phys. Chem. Chem. Phys.* **18**, 18528 (2016).
- ³⁰Y. Ma, J. Cong, and Y. Sun, *J. Phys.: Condens. Matter* **31**, 205701 (2019).
- ³¹W. Li, Z. Wang, F. Deschler, S. Gao, R. H. Friend, and A. K. Cheetham, *Nat. Rev. Mater.* **2**, 16099 (2017).
- ³²Z. Wang, K. Hu, S. Gao, and H. Kobayashi, *Adv. Mater.* **22**, 1526 (2010).
- ³³G. Kresse and J. Hafner, *Phys. Rev. B* **47**, 558 (1993).
- ³⁴G. Kresse and J. Furthmüller, *Comput. Mater. Sci.* **6**, 15 (1996).
- ³⁵G. Kresse and J. Furthmüller, *Phys. Rev. B* **54**, 11169 (1996).
- ³⁶G. Kresse and D. Joubert, *Phys. Rev. B* **59**, 1758 (1999).
- ³⁷J. P. Perdew, K. Burke, and M. Ernzerhof, *Phys. Rev. Lett.* **77**, 3865 (1996).
- ³⁸S. Grimme, *J. Comput. Chem.* **27**, 1787 (2006).
- ³⁹S. Grimme, J. Antony, S. Ehrlich, and H. Krieg, *J. Chem. Phys.* **132**, 154104 (2010).
- ⁴⁰P. S. Ghosh, J. Doherty, S. Lisenkov, and I. Ponomareva, *J. Phys. Chem. C* **125**, 16296 (2021).
- ⁴¹P. S. Ghosh, D. DeTellem, J. Ren, S. Witanachchi, S. Ma, S. Lisenkov, and I. Ponomareva, *Phys. Rev. Lett.* **128**, 077601 (2022).
- ⁴²P. S. Ghosh, S. Lisenkov, and I. Ponomareva, *Phys. Rev. Lett.* **125**, 207601 (2020).
- ⁴³M. Kingsland, P. S. Ghosh, S. Lisenkov, and I. Ponomareva, *J. Phys. Chem. C* **125**, 8794 (2021).
- ⁴⁴R. Kashikar, P. S. Ghosh, S. Lisenkov, B. R. K. Nanda, and I. Ponomareva, *Phys. Rev. B* **104**, 235132 (2021).
- ⁴⁵P. E. Blöchl, *Phys. Rev. B* **50**, 17953 (1994).
- ⁴⁶R. D. King-Smith and D. Vanderbilt, *Phys. Rev. B* **47**, 1651 (1993).
- ⁴⁷D. Vanderbilt and R. D. King-Smith, *Phys. Rev. B* **48**, 4442 (1993).
- ⁴⁸Y. Le Page and P. Saxe, *Phys. Rev. B* **65**, 104104 (2002).
- ⁴⁹S. L. Dudarev, G. A. Botton, S. Y. Savrasov, C. J. Humphreys, and A. P. Sutton, *Phys. Rev. B* **57**, 1505 (1998).
- ⁵⁰M. Cococcioni and S. de Gironcoli, *Phys. Rev. B* **71**, 035105 (2005).
- ⁵¹F. Mouhat and F. X. Coudert, *Phys. Rev. B* **90**, 224104 (2014).
- ⁵²V. Wang, N. Xu, J.-C. Liu, G. Tang, and W.-T. Geng, *Comput. Phys. Commun.* **267**, 108033 (2021).
- ⁵³K.-L. Hu, M. Kurmoo, Z. Wang, and S. Gao, *Chem. - Eur. J.* **15**, 12050 (2009).
- ⁵⁴A. Stroppa, P. Jain, P. Barone, M. Marsman, J. M. Perez-Mato, A. Cheetham, H. Kroto, and S. Picozzi, *Angew. Chem., Int. Ed.* **50**, 5847 (2011).
- ⁵⁵B. Liu, R. Shang, K.-L. Hu, Z.-M. Wang, and S. Gao, *Inorg. Chem.* **51**, 13363 (2012).
- ⁵⁶W. D. C. B. Gunatilleke, K. Wei, Z. Niu, L. Wojtas, G. Nolas, and S. Ma, *Dalton Trans.* **46**, 13342 (2017).
- ⁵⁷S. Chen, R. Shang, K.-L. Hu, Z.-M. Wang, and S. Gao, *Inorg. Chem. Front.* **1**, 83 (2014).
- ⁵⁸K. L. Svane and A. Walsh, *J. Phys. Chem. C* **121**, 421 (2017).
- ⁵⁹G.-C. Xu, W. Zhang, X.-M. Ma, Y.-H. Chen, L. Zhang, H.-L. Cai, Z.-M. Wang, R.-G. Xiong, and S. Gao, *J. Am. Chem. Soc.* **133**, 14948 (2011).
- ⁶⁰G.-C. Xu, X.-M. Ma, L. Zhang, Z.-M. Wang, and S. Gao, *J. Am. Chem. Soc.* **132**, 9588 (2010).
- ⁶¹M. Maczka, A. Pietraszko, B. Macalik, and K. Hermanowicz, *Inorg. Chem.* **53**, 787 (2014).
- ⁶²L. Mazzuca, L. Cañadillas-Delgado, O. Fabelo, J. A. Rodríguez-Velamazán, J. Luzón, O. Vallcorba, V. Simonet, C. V. Colin, and J. Rodríguez-Carvajal, *Chem. - Eur. J.* **24**, 388 (2018).
- ⁶³R. Shang, X. Sun, Z.-M. Wang, and S. Gao, *Chem. - Asian J.* **7**, 1697 (2012).
- ⁶⁴B. Pato-Doldán, L. C. Gómez-Aguirre, A. P. Hansen, J. Mira, S. Castro-García, M. Sánchez-Andújar, M. A. Señaris-Rodríguez, V. S. Zapf, and J. Singleton, *J. Mater. Chem. C* **4**, 11164 (2016).
- ⁶⁵L. Hu, Z. Wang, H. Wang, Z. Qu, and Q. Chen, *RSC Adv.* **8**, 13675 (2018).
- ⁶⁶M. Maczka, A. Ciupa, A. Gagor, A. Sieradzki, A. Pikul, B. Macalik, and M. Drozd, *Inorg. Chem.* **53**, 5260 (2014).
- ⁶⁷Hybrid-formate-perovskites," <https://github.com/USFmatscilab/Hybrid-Formate-Perovskites> (2023).
- ⁶⁸G. Kieslich, S. Kumagai, K. T. Butler, T. Okamura, C. H. Hendon, S. Sun, M. Yamashita, A. Walsh, and A. K. Cheetham, *Chem. Commun.* **51**, 15538 (2015).
- ⁶⁹N. A. Spaldin, *J. Solid State Chem.* **195**, 2 (2012), part of Special Issue: polar Inorganic Materials: Design Strategies and Functional Properties.
- ⁷⁰S. Hu, H. Gao, Y. Qi, Y. Tao, Y. Li, J. R. Reimers, M. Bokdam, C. Franchini, D. Di Sante, A. Stroppa, and W. Ren, *J. Phys. Chem. C* **121**, 23045 (2017).
- ⁷¹D. Di Sante, A. Stroppa, P. Jain, and S. Picozzi, *J. Am. Chem. Soc.* **135**, 18126 (2013).
- ⁷²I. E. Collings, M. Bykov, E. Bykova, M. G. Tucker, S. Petitgirard, M. Hanfland, K. Glazyrin, S. van Smaalen, A. L. Goodwin, L. Dubrovinsky, and N. Dubrovinskaia, *CrystEngComm* **18**, 8849 (2016).
- ⁷³Y. Sun, Z. Zhuo, and X. Wu, *RSC Adv.* **6**, 113234 (2016).
- ⁷⁴A. Stroppa, P. Barone, P. Jain, J. M. Perez-Mato, and S. Picozzi, *Adv. Mater.* **25**, 2284 (2013).
- ⁷⁵P. C. Rout and V. Srinivasan, *Phys. Rev. Mater.* **2**, 014407 (2018).
- ⁷⁶C. Capillas, E. S. Tasci, G. de la Flor, D. Orobengoa, J. M. Perez-Mato, and M. I. Aroyo, *Z. Kristallogr.* **226**, 186 (2011).
- ⁷⁷C. M. Acosta, A. Fazzio, G. M. Dalpian, and A. Zunger, *Phys. Rev. B* **102**, 144106 (2020).
- ⁷⁸T. E. Smidt, S. A. Mack, S. E. Reyes-Lillo, A. Jain, and J. B. Neaton, *Sci. Data* **7**, 72 (2020).
- ⁷⁹D. Mainprice, F. Bachmann, R. Hielscher, H. Schaeben, and G. E. Lloyd, *Geol. Soc. Spec. Publ.* **409**, 223 (2015).
- ⁸⁰N. H. Yusoff, R. A. M. Osman, M. S. Idris, K. N. D. K. Muhsen, and N. I. M. Nor, *AIP Conf. Proc.* **2203**, 020038 (2020).
- ⁸¹M. Born, *Math. Proc. Cambridge Philos. Soc.* **36**, 160–172 (1940).
- ⁸²V. Woldemar, *Lehrbuch Der Kristallphysik (Mit Ausschluss Der Kristalloptik)* (B.G. Teubner, Leipzig, Berlin, 1928), pp. 1–978.
- ⁸³R. Hill, *Proc. Phys. Soc., London, Sect. A* **65**, 349 (1952).
- ⁸⁴A. Reuss, *Z. Angew. Math. Mech.* **9**, 49 (1929).

- ⁸⁵O. L. Anderson, *J. Phys. Chem. Solids* **24**, 909 (1963).
- ⁸⁶X. Q. Chen, H. Niu, D. Li, and Y. Li, *Intermetallics* **19**, 1275 (2011).
- ⁸⁷Y. Tian, B. Xu, and Z. Zhao, *Int. J. Refract. Met. Hard Mater.* **33**, 93 (2012).
- ⁸⁸J. Islam and A. K. M. A. Hossain, *RSC Adv.* **10**, 7817 (2020).
- ⁸⁹M. S. Hossain, M. M. Haque Babu, T. Saha, M. S. Hossain, J. Podder, M. S. Rana, A. Barik, and P. Rani, *AIP Adv.* **11**, 055024 (2021).
- ⁹⁰D. Gui, L. Ji, A. Muhammad, W. Li, W. Cai, Y. Li, X. Li, X. Wu, and P. Lu, *J. Phys. Chem. Lett.* **9**, 751 (2018).
- ⁹¹G. Kieslich, A. C. Forse, S. Sun, K. T. Butler, S. Kumagai, Y. Wu, M. R. Warren, A. Walsh, C. P. Grey, and A. K. Cheetham, *Chem. Mater.* **28**, 312 (2016).
- ⁹²M. Viswanathan, *J. Phys. Chem. C* **123**, 6711 (2019).
- ⁹³J. M. Ogborn, I. E. Collings, S. A. Moggach, A. L. Thompson, and A. L. Goodwin, *Chem. Sci.* **3**, 3011 (2012).
- ⁹⁴M. Sánchez-Andújar, S. Presedo, S. Yáñez-Vilar, S. Castro-García, J. Shamir, and M. A. Señaris-Rodríguez, *Inorg. Chem.* **49**, 1510 (2010).
- ⁹⁵N. Abhyankar, J. J. Kweon, M. Orío, S. Bertaina, M. Lee, E. S. Choi, R. Fu, and N. S. Dalal, *J. Phys. Chem. C* **121**, 6314 (2017).